Volume 50 Issue 1 January 2012   ISSN 0263-8231

ELSEVIER

THIN-WALLED STRUCTURES

Editor
J. LOUGHLAN

North American Editor
K.P. CHONG

THIN-WALLED
STRUCTURES

www.elsevier.com/locate/tws

Available online at www.sciencedirect.com
SciVerse ScienceDirect

(This is a sample cover image for this issue. The actual cover is not yet available at this time.)
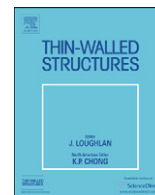
Nonlinear dynamics of rotating box FGM beams using nonlinear normal modes

Sebastián P. Machado [a,b,*], Marcelo T. Piovan [a,b]

[a] Grupo Análisis de Sistemas Mecánicos, Centro de Investigaciones de Mecánica Teórica y Aplicada, Universidad Tecnológica Nacional FRBB,
11 de Abril 461, B8000LMI Bahía Blanca, Argentina
[b] Consejo Nacional de Investigaciones Científicas y Tecnológicas. Argentina

ARTICLE INFO

ABSTRACT

In this work an analysis is performed on the nonlinear planar vibrations of a functionally graded beam subjected to a combined thermal and harmonic transverse load in the presence of internal resonance. Adopting the direct perturbation MMS technique, the partial differential equations of motion of the beam are reduced to sets of first-order nonlinear modulation equations in terms of the complex modes of the beam. The assumption of steady-state values of centrifugal loads is evaluated. It has to be said that there is a lack of information about modeling of rotating box beams made of functionally graded materials (FGMs) under thermo-mechanical loads. The influence of the transverse load amplitude and the internal detuning parameter on the strength of nonlinear modal interaction is illustrated. It is also shown that the system exhibits periodic and quasiperiodic responses for a typical range of parameter values.

© 2012 Published by Elsevier Ltd.

1. Introduction

The problem of modeling and studding of a rotating flexible beam has received a constant research interest in connection with the applications like flexible robot arms, rotor blades and spacecraft with flexible appendages. The most simplified representation of a rotating beam is a one-dimensional Euler–Bernoulli model. A uniform rotating beam of doubly symmetric cross-section is a special case. Owing to the stiffening effect of the centrifugal tension, one generally can expect the natural frequencies to increase with an increase in the speed of rotation. Several works have studied a rotating cantilever beam and approximate methods such as Rayleigh–Ritz, Galerkin, finite element methods, etc., has been used to find the natural frequencies [1–4]. However, the internally resonant analysis of rotating beams is rather rare in the literature [5–8]. Systematic procedures have been developed to obtain reduced-order models (ROMs) via nonlinear normal modes (NNMs) that are based on invariant manifolds in the state space of nonlinear systems [9–12]. These procedures initially used asymptotic series to approximate the geometry of the invariant manifold. They have been used by Pesheck et al. [5] to study the nonlinear rotating Euler–Bernoulli beam. Also, Pesheck et al. [6] employed a numerically-based Galerkin approach to generate accurate reduced-order models for large-amplitude, strongly non-linear motions.

Apiwattanalunggarn et al. [7] presented a nonlinear one-dimensional finite-element model representing the axial and transverse motions of a cantilevered rotating beam, which is reduced to a single nonlinear normal mode using invariant manifold techniques. They used this approach to study the dynamic characteristics of the finite element model over a wide range of vibration amplitudes. It is interesting to note that the interest of most works about nonlinear dynamic of rotating beams have focused on the reduced-order model as the invariant manifold solution. Turhan and Bulut [8] investigated the in-plane nonlinear vibrations of a rotating beam via single- and two-degree-of-freedom models obtained through a Galerkin discretization. They performed a perturbation analyses on single- and two-degree-of-freedom models to obtain amplitude dependent natural frequencies and frequency responses.

On the other hand, there are many papers concerning mechanics of beams made of FGMs. In the opinion of the authors, the articles presented in [13–15] among others offer interesting features, applications and calculation methodologies. These models are developed by means of different constitutive hypotheses (graded metallic-ceramic, graded multilayered, etc.) and displacement formulation (i.e. elementary Bernoulli–Euler or Timoshenko or Higher order shear deformable theories). The constitutive modeling is commonly related to a classical rule of mixtures and the material properties vary according to a power law expression [14] or an exponential expression [13].

Now, taking into account the technological context, it is important to mention that there is a lack of information about rotating beams constructed with FGMs. Piovan and Sampaio [16]

* Corresponding author. Tel.: +54 0291 4555220.
E-mail addresses: smachado@frbb.utn.edu.ar (S.P. Machado),
mpiovan@frbb.utn.edu.ar (M.T. Piovan).

introduced a nonlinear model for planar analysis of rotating beams with material properties graded along the solid cross-section. Only a few authors explored in recent years the dynamics of thin-walled beams constructed with functionally graded materials. Piovan and Sampaio [17] developed a theory to study the dynamics of telescopic thin walled beams made of FGMs. Oh et al. [18,19] introduced a couple of first-order-shear models to study vibratory patterns of spinning and rotating thin-walled beams constructed with FGMs. The papers given by Fazelzadeh et al. [20] and Fazelzadeh and Hosseini [21] also deal with rotating beams made of FGMs. However in these formulations no geometrical stiffness has been taken into account. The interest of these papers has been focused in the thermoelastic effects related to graded properties.

From the review of literature, it is found that the study of internal resonance in the area of cantilever rotating slender beam subjected to a harmonic transverse load has not yet been explored so far, neither in the context of composite materials nor in the context of functionally graded materials. The nonlinear modal interaction or the internal resonance in the system arising out of commensurable relationships of frequencies, in presence of parametric excitation due to periodic load can have possible influence on system behavior, which needs to be studied.

In the present paper, the nonlinear planar vibration of a rotating FGMs cantilever beam is analyzed, considering the dynamic condition of internal resonance. The model is based on a one-dimensional Euler–Bernoulli formulation where the geometric cubic nonlinear terms (due to midline stretching of the beam) are included in the equation of motion. The linear frequencies of the system are dependent on the rotation speed; this effect is used to activate the internal resonance. For a particular rotation speed the second natural frequency is approximately three times the first natural frequency and hence the first and second modes may interact due to a three-one internal resonance. Principal parametric resonance of first mode considering internal resonance is also analyzed. For a comprehensive review of nonlinear modal interactions, we refer the reader to [22–24]. The method of multiple scales (MMS) is used to attack directly the governing nonlinear partial differential equation of motion of the beam and reduce the problem to sets of first-order nonlinear modulation equations in terms of the complex modes of the beam [25]. These modulation equations are numerically analyzed for stability and bifurcations of trivial and nontrivial solutions. Bifurcation diagrams representing system responses with variation of parameters like amplitude and frequency of the lateral excitation load, frequency detuning of internal resonances and damping are computed with the help of a continuation algorithm [26]. The trivial state stability plots are presented and the modulation equations are numerically integrated to obtain the dynamic solutions (periodic, quasiperiodic and chaotic responses) for typical system parameters.

For the principal parametric resonance of first mode, the influence of internal resonance is illustrated in the frequency and amplitude responses. The system is shown to have Hopf and saddle node bifurcations for different parameter values. The influence of intensity of transverse load amplitude and frequency detuning for internal resonance on the strength of nonlinear modal interaction is illustrated. The system exhibits dynamic solutions like periodic and quasiperiodic responses for typical range of parameter values.

2. Funcionally graded material and its thermal properties

The laws of variation of the material properties along the wall thickness can be prescribed in order to bear in mind for different types of material gradation such as metal to ceramic or metal to metal (e.g. steel and aluminum). In this case, a simple gradation

based on a power-law is employed. The law of variation of the elastic and mass properties along the wall-thickness e is:

$$P(n) = P_M + (P_C - P_M)\left(\frac{2n+e}{2e}\right)^K \tag{1}$$

where $P(n)$ denotes a typical material property (i.e., density ρ or Young's modulus E or Poisson coefficient v). Sub-indexes C and M define the properties of the material of the outer surface (normally ceramic) and inner surface (normally metallic), respectively. The exponent K, which is connected to the ratio of constituents in volume, can have different values that may vary between zero (i.e., a full ceramic phase) or infinity (i.e., a full metallic phase).

It is assumed that the beam is subjected to a steady-state one dimensional (1-D) temperature distribution through its thickness. The steady-state 1-D heat transfer equation is expressed by:

$$\frac{d}{dn}\left[k(n)\frac{dT}{dn}\right] = 0 \tag{2}$$

where k is the coefficient of the thermal conduction. The boundary conditions are:

$$T = T_M \text{ at } n = -\frac{e}{2} \text{ and } T = T_C \text{ at } n = \frac{e}{2} \tag{3}$$

The solution of Eq. (2) can be obtained by means of the polynomial series. Therefore, $T(n)$ is calculated as [27]:

$$T(n) = T_M + \frac{\Delta T}{\eta} \sum_{j=0}^{\psi} (-1)^j \frac{(k_C - k_M)^j}{(1+jK)k_M^j}\left(\frac{n}{e} + \frac{1}{2}\right)^{(1+jK)} \tag{4}$$

with

$$\eta = \sum_{j=0}^{\psi} (-1)^j \frac{(k_C - k_M)^j}{(1+jK)k_M^j} \tag{5}$$

where normally the upper limit of the summation is $\Psi \to \infty$, however by means of an elemental numerical study one can prove that Eq. (4) may be finely approximated by taking just a few terms, or more practically, $\Psi \geq 5$ as it was done by many researchers [28].

Throughout the numerical simulation T_M is taken 300 K. It is assumed that the properties of the FGMs are temperature-dependent and vary according to a law obtained experimentally. These are expressed in a general form as [19,29]:

$$p(n) = p_0(p_{-1}/T + 1 + p_1 T + p_2 T^2 + p_3 T^3) \tag{6}$$

in which p is a temperature-varying material property in general (i.e. modulus of elasticity, or Poisson's coefficient, etc.), T is the absolute temperature [°K] and the coefficient p_i is unique for a particular material and obtained by means of a curve fitting procedure. Thus the material properties can be represented as a function of the thickness and the temperature. It is clear that p_0 is the typical material property in absence of thermal effects.

3. Non-linear equations of motion

In this section the nonlinear equations of motion of a rotating box beam subjected to harmonic transverse loads are presented. The structural model of a thin-walled beam is shown in Fig. 1. The origin of the beam coordinate system (x, y, z) is located at the blade root at an offset R_0 from a rotation axis fixed in space. R_0 denotes the radius of the hub (considered to be rigid) in which the blade or beam is mounted. The hub rotates about its polar axis through the origin 0. We assume that the motion is planar and the cross sections remains plane during transverse bending. A doubly symmetric cross-section box-beam is used, thus uncoupling the out-of-plane (flapping) and in-plane (lead-lag) vibration.

Following the mathematical formulation developed by the authors in [30], considering in this case a Bernoulli–Euler theory
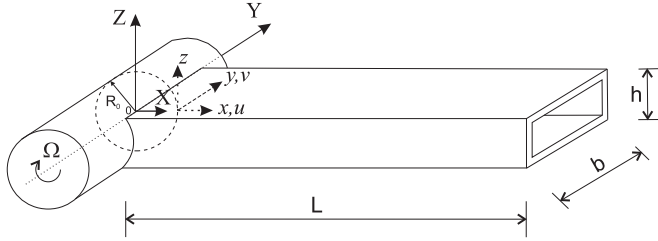
Fig. 1. Schematic description of the rotating box beam.

and adding the rotation effect, the governing differential equations of a FGMs beam is given by

$$-Q'_x + M_1(x) - J^{\rho}_{11}(R_0 + x + u)\Omega^2 = 0 \tag{7}$$

$$M_z'' - (Q_x v')' + M_2(x) = F(x)\cos(\varpi t) \tag{8}$$

In Eqs. (7) and (8) primes mean derivation with respect to the space variable x. The variable u is the axial displacement of the cross-section, v is the lateral displacements and Ω is the beam rotation speed. On the other hand, Q_x is the axial force and M_z is the bending moment. $F(x)$ describes the spatial distribution of the applied transverse harmonic load and ϖ is the excitation frequency. Finally, M_1 and M_2 are the inertia forces. These inertia forces can be expressed in terms of the accelerations as follows:

$$M_1 = J^{\rho}_{11}\ddot{u}, \tag{9}$$

$$M_2 = J^{\rho}_{11}\ddot{v} \tag{10}$$

where $J^{\rho}_{11} = \int_A \rho(n)ds dn$, ρ is the graded mass density.

The beam forces involved in Eqs. (7) and (8) can be defined in terms of the shell-stress resultants in the following form:

$$Q_x = \int_S N_{xx}ds, \tag{11}$$

$$M_z = \int_s \left(N_{xx}\overline{Y} - M_{xx}\frac{dZ}{ds}\right)ds. \tag{12}$$

From the conventional definitions of shell stress-resultants given by

$$N_{xx} = \int_{-e/2}^{e/2}\sigma_{xx}dn \tag{13}$$

$$M_{xx} = \int_{-e/2}^{e/2}\sigma_{xx}n\,dn \tag{14}$$

Functionally graded shells are usually considered to be composed by many isotropic homogeneous layers [31]. Thus, the stress–strain relation for a generally isotropic material including thermal effects is expressed as

$$\sigma_{xx} = \frac{E_f}{1-v_f^2}\varepsilon_{xx} - \frac{E_f}{1-v_f}\alpha_f\Delta T \tag{15}$$

in which E_f, v_f, and α_f are the graded modulus of elasticity, Poisson's coefficient and thermal expansion coefficient, respectively. These properties are defined in $n\,\varepsilon\,[-e/2, e/2]$, according to the power law defined in Eq. (1).

Substituting Eq. (15) into Eqs. (13) and (14), after an algebraic rearrangement it is possible to derive the following constitutive equation of shell-forces accounting for thermal effects:

$$\begin{Bmatrix} N_{xx} \\ M_{xx} \end{Bmatrix} = \begin{bmatrix} \overline{A}_{11} & \overline{B}_{11} \\ \overline{B}_{11} & \overline{D}_{11} \end{bmatrix}\begin{Bmatrix} \varepsilon_{xx} \\ \kappa_{xx} \end{Bmatrix} - \begin{bmatrix} \overline{T}_{NN} & \overline{T}_{NM} \\ \overline{T}_{NM} & \overline{T}_{MM} \end{bmatrix}\begin{Bmatrix} Q_N^{(T)} \\ Q_M^{(T)} \end{Bmatrix} \tag{16}$$

where $\overline{A}_{ij}$, $\overline{B}_{ij}$, $\overline{D}_{ij}$, $\overline{T}_{NN}$, $\overline{T}_{NM}$ and $\overline{T}_{MM}$ are modified elastic and thermal expansion coefficients, whose definitions can be followed

in [30]. On the other hand, ε_{xx} and κ_{xx} are normal strains and curvature of the shell, whereas $Q_N^{(T)}$ and $Q_M^{(T)}$ are defined according to

$$\begin{Bmatrix} Q_N^{(T)} \\ Q_M^{(T)} \end{Bmatrix} = \int_{-e/2}^{e/2}\alpha_f\frac{E_f}{1-v_f}\Delta T\begin{Bmatrix} 1 \\ n \end{Bmatrix}dn \tag{17}$$

The shell strains ε_{xx} and κ_{xx} can be expressed in the following form:

$$\varepsilon_{xx} = u' + \frac{1}{2}v'^2 + \overline{Y}v'', \; \kappa_{xx} = \frac{dZ}{ds}v'' \tag{18}$$

Now taking into account the definition of the beam forces given in Eqs. (11) and (12) and employing the definitions of shell forces and strains given in Eqs. (16) and (18), the expression of the generalized beam forces are obtained as in [30].

Substituting the generalized beam forces in Eqs. (7) and (8), neglecting the inertial effects along the longitudinal direction and following Nayfeh et al. [32], the equation of motion governing the transverse deflection $v(x,t)$ is written as

$$J^{\rho}_{11}\ddot{v} + EIv^{iv} - EA\left[\frac{1}{2L}\int_0^L v'^2 dx + \frac{J^{\rho}_{11}}{EA}\Omega^2\left(\frac{L^2}{6} - \frac{x^2}{2} + R_0\frac{L}{2} - R_0 x\right) - \overline{Q}_T\right]v''$$
$$+ J^{\rho}_{11}\Omega^2 v'(x + R_0) = F(x)\cos(\varpi t) \tag{19}$$

where EA and EI are the axial and flexural rigidity and $\overline{Q}_T = \alpha\Delta T$. Overdots indicate differentiation with respect to time and primes with respect to the axial co-ordinate. In this case, for a rotating cantilever beam, boundary conditions demand that

$$v = 0 \text{ and } v' = 0 \text{ at} x = 0$$
$$v'' = 0 \text{ and } v''' = 0 \text{ at} x = L \tag{20}$$

Finally, introducing nondimensional quantities

$$t^* = \sqrt{\frac{EI}{L^4 J^{\rho}_{11}}}t, \; x^* = \frac{x}{L} \tag{21}$$

Substituting the relationships Eq. (21) into Eq. (19), adding damping μ and dropping the asterisk, the expressions can be conveniently rewritten as

$$\ddot{v} - \chi v'' + v^{iv} + 2\mu\dot{v} - \gamma v''\int_0^L v'^2 dx + \lambda v' = f\cos(\varpi t) \tag{22}$$

$$v = 0 \text{ and } v' = 0 \text{ at } x = 0,$$
$$v'' = 0 \text{ and } v''' = 0 \text{ at } x = 1, \tag{23}$$

where

$$\gamma = \frac{EA}{2EI}, \; \lambda = \overline{\Omega}^2\left(\frac{1}{2} + \frac{R_0}{L}\right), \; f = \frac{F(x)}{EI}L^4, \; \overline{\Omega}^2 = \Omega^2\frac{J^{\rho}_{11}}{EI}L^4,$$
$$\chi = \left[\frac{J^{\rho}_{11}}{EI}L^2\left(\frac{L^2}{6} + R_0\frac{L}{2}\right)\Omega^2 - L^2\frac{EA}{EI}\overline{Q}_T\right] \tag{24}$$

4. Method of analysis

The MMS is applied directly to the partial differential Eq. (22) and the associated boundary conditions Eq. (23) in order to analyze the present system of rotating cantilever beam. This technique presents some advantage over the discretization perturbation technique [22,24]. We seek an approximate solution to this weakly nonlinear distributed parameter system in the form of a first-order uniform expansion and introduce the time scale

$T_n = \varepsilon^n t$, $n = 0,1,2,\ldots$ The time derivatives are

$$\frac{d}{dt} = D_0 + \varepsilon D_1 + \ldots, \quad \frac{d^2}{dt^2} = D_0^2 + 2\varepsilon D_0 D_1 + \ldots, D_0 = \frac{\partial}{\partial T_n}, \quad n = 0,1,2,\ldots$$

(25)

A small parameter ε is introduced by ordering the linear damping and load amplitude as $\mu = \varepsilon\tilde{\mu}$, $f = \varepsilon\tilde{f}$. Moreover, the displacement $v(x,t)$ are expanded as:

$$v(x,t) = v_1(T_0, T_1, x) + \varepsilon v_2(T_0, T_1, x) + \ldots$$

(26)

Substituting Eqs. (25) and (26) into Eqs. (22) and (23) and equating coefficients of like powers of ε on both sides, we obtain

Order ε^0

$$D_0^2 v_1 + v_1^{iv} - \chi v_1'' + \lambda v_1' = 0$$

(27)

$$v_1 = 0, \; v_1' = 0 \text{ at } x = 0$$

(28)

$$v_1'' = 0, \; v_1''' = 0 \text{ at } x = 1$$

(29)

Order ε^1:

$$D_0^2 v_2 + v_2^{iv} - \chi v_2'' + \lambda v_2' = -2D_0 D_2 v_2 - 2\mu D_0 v_1 - \gamma v_1'' \int_0^1 {v_1'}^2 dx + f\cos(\varpi t)$$

(30)

$$v_2 = 0, \; v_2' = 0 \text{ at } x = 0$$

(31)

$$v_2'' = 0, \; v_2''' = 0 \text{ at } x = 1$$

(32)

The solution to the first-order perturbation Eqs. (27–29) can be expressed as

$$v_1(T_0, T_1, x) = \sum_{m=1}^{\infty} \phi_m(x) A_m(T_1) e^{i\omega_m T_0} + cc$$

(33)

where $\phi_m(x)$ is the mode shape, ω_m is the natural frequency and cc stands for complex conjugate. The mode shape $\phi_m(x)$ for the specified cantilever boundary conditions is calculated as

$$\begin{aligned}
\phi_m(x) = e^{x\beta_{4m}} &+ \Big\{ e^{x\beta_{3m}}[-e^{\beta_{2m}}\beta_{2m}^2(\beta_{1m}-\beta_{4m}) + e^{\beta_{1m}}\beta_{1m}^2(\beta_{2m}-\beta_{4m}) \\
&+ e^{\beta_{4m}}\beta_{4m}^2(\beta_{1m}-\beta_{2m})] + e^{x\beta_{2m}}[e^{\beta_{3m}}\beta_{3m}^2(\beta_{1m}-\beta_{4m}) \\
&- e^{\beta_{1m}}\beta_{1m}^2(\beta_{3m}-\beta_{4m}) - e^{\beta_{4m}}\beta_{4m}^2(\beta_{1m}-\beta_{3m})] \\
&+ e^{x\beta_{1m}}[-e^{\beta_{3m}}\beta_{3m}^2(\beta_{2m}-\beta_{4m}) + e^{\beta_{2m}}\beta_{2m}^2(\beta_{3m}-\beta_{4m}) \\
&+ e^{\beta_{4m}}\beta_{4m}^2(\beta_{2m}-\beta_{3m})] \Big\} / [-e^{\beta_{2m}}\beta_{2m}^2 \\
&(\beta_{1m}-\beta_{3m}) + e^{\beta_{1m}}\beta_{1m}^2(\beta_{2m}-\beta_{3m}) + e^{\beta_{3m}}\beta_{3m}^2(\beta_{1m}-\beta_{2m})]
\end{aligned}$$

(34)

where β_{im} is the eigenvalue which satisfies the relation

$$\beta_{im}^4 - \chi\beta_{im}^2 + \lambda\beta_{im} - \omega_m^2 = 0 \; , i = 1,2,3,4$$

(35)

and the characteristic equation

$$\begin{aligned}
(\beta_{2n}-\beta_{3n})(\beta_{1m}-\beta_{4m})&(e^{\beta_{2n}+\beta_{3n}}\beta_{2n}^2\beta_{3n}^2 + e^{\beta_{1n}+\beta_{4n}}\beta_{1n}^2\beta_{4n}^2) \\
+ (\beta_{1n}-\beta_{3n})(\beta_{2m}-\beta_{4m})&(-e^{\beta_{1n}+\beta_{3n}}\beta_{1n}^2\beta_{3n}^2 - e^{\beta_{2n}+\beta_{4n}}\beta_{2n}^2\beta_{4n}^2) \\
+ (\beta_{1n}-\beta_{2n})(\beta_{3m}-\beta_{4m})&(e^{\beta_{1n}+\beta_{2n}}\beta_{1n}^2\beta_{2n}^2 + e^{\beta_{3n}+\beta_{4n}}\beta_{3n}^2\beta_{4n}^2) = 0
\end{aligned}$$

(36)

The natural frequencies of the cantilever beam vary with the rotation speed. For specific combinations of system parameters, the lower natural frequencies can be commensurable, leading to internal resonance in the system and nonlinear interaction between the associated modes. A three-to-one internal resonance $\omega_2 \cong 3\omega_1$ is considered for a range of rotation beam speed and it is assumed that there is no other commensurable frequency relationship with higher modes. Therefore Eq. (33) is replaced by

$$v_1(T_0, T_1, x) = A_1(T_1)\phi_1(x)e^{i\omega_1 T_0} + A_2(T_1)\phi_2(x)e^{i\omega_2 T_0} + cc$$

(37)

where A_i is the unknown complex-valued function.

Now, in order to investigate the system response under internal and external resonance conditions, two detuning parameters σ_i are

introduced:

$$\omega_2 = 3\omega_1 + \varepsilon\sigma_1, \quad \varpi = \omega_1 + \varepsilon\sigma_2.$$

(38)

Substituting Eqs. (37) and (38) to find the solution of Eq. (30), we obtain

$$\begin{aligned}
D_0^2 v_2 + v_2^{iv} - \chi v_2'' + \lambda v_2' &= \Gamma_1(T_1, x)e^{i\omega_1 T_0} + \Gamma_2(T_1, x)e^{i(3\omega_1 T_0 + \sigma_1 T_1)} \\
&+ \frac{1}{2}f e^{i(\omega_1 T_0 + \sigma_1 T_2)} + cc + NST
\end{aligned}$$

(39)

where the term Γ_m is defined in the Appendix and NST stands for terms that do not produce secular or small divisor terms. As the homogeneous part of Eq. (39) with its associated boundary conditions has a nontrivial solution, the corresponding non-homogeneous problem has a solution only if a solvability condition is satisfied [22]. This requires the right-hand side of Eq. (39) to be orthogonal to every solution of the adjoint homogeneous problem, which leads to the following complex variable modulation equations for the amplitude and phase

$$2i(A_1' + \mu_1 A_1) + 8A_1(\gamma_{11}A_1\overline{A}_1 + \gamma_{12}A_2\overline{A}_2) + 8\delta_1 A_2\overline{A}_1^2 e^{i\sigma_1 T_1} - \frac{1}{2}f_1 e^{i\sigma_2 T_1} = 0$$

(40)

$$2i(A_2' + \mu_2 A_2) + 8A_2(\gamma_{21}A_1\overline{A}_1 + \gamma_{22}A_2\overline{A}_2) + 8\delta_2 A_1^3 e^{-i\sigma_1 T_1} = 0$$

(41)

where prime denotes differentiation with respect to the slow time T_1 and μ_m, γ_m, δ_m and f_1 are defined in Appendix. Overbar indicates complex conjugate amplitude. It is interesting to note that the terms in the above equations involving the internal frequency detuning parameter σ_1 constitute the contributions of internal resonance in the system.

Introducing a Cartesian transformation

$$A_k = \frac{1}{2}\left[p_k(T_1) - iq_k(T_1)\right]e^{i\nu_k T_1}, \; k = 1,2$$

(42)

into the Eqs. (40) and (41), the following amplitude and phase expressions are obtained:

$$\begin{aligned}
p_1' = &-\mu_1 p_1 - \nu_1 q_1 + \gamma_{11}q_1(p_1^2 + q_1^2) \\
&+ \gamma_{12}q_1(p_2^2 + q_2^2) - \delta_1[2p_1 q_1 p_2 - q_2(p_1^2 + q_1^2)]
\end{aligned}$$

(43)

$$\begin{aligned}
q_1' = &-\mu_1 q_1 + \nu_1 p_1 - \gamma_{11}p_1(p_1^2 + q_1^2) - \gamma_{12}p_1(p_2^2 + q_2^2) \\
&- \delta_1\left[2p_1 q_1 q_2 + p_2(p_1^2 - q_1^2)\right] + \frac{1}{2}f_1
\end{aligned}$$

(44)

$$\begin{aligned}
p_2' = &-\mu_2 p_2 - \nu_2 q_2 + \gamma_{21}q_2(p_1^2 + q_1^2) + \gamma_{22}q_2(p_2^2 + q_2^2) \\
&+ \delta_2 q_1(3p_1^2 - q_1^2)
\end{aligned}$$

(45)

$$\begin{aligned}
q_2' = &-\mu_2 q_2 + \nu_2 p_2 - \gamma_{21}p_2(p_1^2 + q_1^2) - \gamma_{22}p_2(p_2^2 + q_2^2) \\
&+ \delta_2 p_1(3q_1^2 - p_1^2)
\end{aligned}$$

(46)

where

$$\nu_1 = \sigma_2, \; \nu_2 = 3\sigma_2 - \sigma_1$$

(47)

and the prime indicates the derivative with respect to T_1.

5. Results and discussion

For the analysis of the rotating beam subjected to principal parametric resonance of the first mode (i.e., $\varpi \cong \omega_1$) in presence of 3:1 internal resonance, system parameters are taken as mentioned earlier corresponding to the commensurable natural frequencies of the first and second mode of the system. There are no modal interactions involving other modes. The beam geometrical characteristics used in this analysis are the same employed by others authors [21]: $L = 1.2$ m, $h = 0.0827$ m, $b = 0.257$ m, $e = 0.01654$ m and $R_0 = 1.3$ m. The closed box beam is constructed with a metallic alloy

(Ti6Al4V) and a ceramic (ZrO2), whose properties are given in Table 1.

For a volume fraction exponent $K=1$ and $T_C=600$ K, the internal resonance is perfectly tuned when $\overline{\Omega}=4.607$. The following dimensionless parameter has been considered in the numerical simulations

$$\overline{\omega}_i^2 = \omega_i^2 \frac{\rho A}{EI} L^4 \qquad (48)$$

where ω_i is the ith natural frequency of the beam obtained from Eq. (36). The second natural frequency and three times the first natural frequency are plotted as functions of $\overline{\Omega}$ in Fig. 2. In the case of $\overline{\Omega}=4.607$, the scaled natural frequencies are $\overline{\omega}_1=8.9$ and $\overline{\omega}_2=26.7$. The corresponding nonlinear interaction coefficients, defined in Eqs. (43)–(46), for the specified rotating speed are: $\gamma_{11}=15.40$, $\gamma_{12}=1353.19$, $\gamma_{21}=-176.485$, $\gamma_{22}=-2780.57$, $\delta_1=-135.43$ and $\delta_2=5.56$.

5.1. Steady-state motions and stability

The equilibrium solutions of Eqs. (43)–(46) correspond to periodic motions of the beam. Steady-state solutions are determined by setting $p_i'=q_i'=0$ the right-hand members of the modulation Eqs. (43)–(46) and solving the non-linear system. Stability analysis is then performed by analyzing the eigenvalues of the Jacobian matrix of the non-linear equations calculated at the fixed points. Amplitude-load curves are reported in Fig. 3, for a damping values $\mu_1=\mu_2=0.05$ and considering different resonance conditions. The amplitudes a_1 and a_2 are obtained by means of the following expression:

$$a_i = \sqrt{p_i^2 + q_i^2}, \ i=1,2 \qquad (49)$$

In the case of perfect resonance condition ($\sigma_1=\sigma_2=0.04$), the modal solution is stable for all load conditions. However, for a

Table 1
Temperature dependant coefficients of material properties for ceramic (ZrO$_2$) and metals (Ti–6Al–4V).

	Material	P_{-1}	P_0	P_1	P_2	P_3
E (Pa)	Ti–6Al–4V	0	122.7×10^9	-4.605×10^{-4}	0	0
	ZrO$_2$	0	132.2×10^9	-3.805×10^{-4}	-6.127×10^{-8}	0
ν	Ti–6Al–4V	0	0.2888	1.108×10^{-4}	0	0
	ZrO$_2$	0	0.3330	0	0	0
ρ (kg/m^3)	Ti–6Al–4V	0	4420	0	0	0
	ZrO$_2$	0	3657	0	0	0
α (1/K)	Ti–6Al–4V	0	7.43×10^{-6}	7.483×10^{-4}	-3.621×10^{-7}	0
	ZrO$_2$	0	13.3×10^{-6}	-1.421×10^{-3}	9.549×10^{-7}	0
k (W/mK)	Ti–6Al–4V	0	6.10	0	0	0
	ZrO$_2$	0	1.78	0	0	0
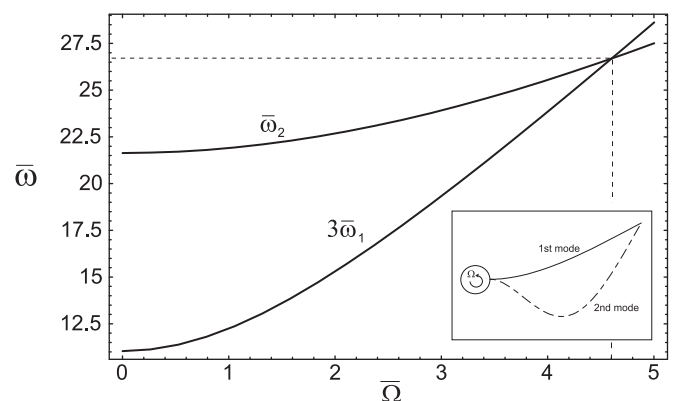
Fig. 2. Variations of three times the first $\overline{\omega}_1$ and second $\overline{\omega}_2$ scaled natural frequencies with $\overline{\Omega}$.
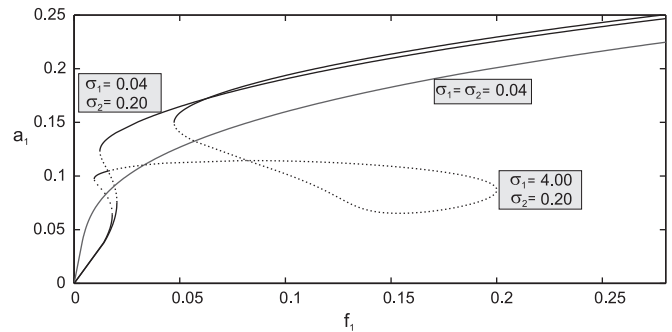

Fig. 3. Amplitude–load curves for the first modal response. Thick line: stable solutions; dashed line: unstable solutions.

small value of the external detuning parameter ($\sigma_2=0.2$), the amplitude modal branch alternatively loses and regains stability due to the presence of some saddle-nodes bifurcations. On the other hand, when the internal detuning parameter is far from the perfect resonance condition ($\sigma_1=4$), the solution presents some stable and unstable branches.

The frequency–response curves are shown in Fig. 4a and b, for a particular internal resonance condition. The modal amplitude a_i curves are obtained as a function of the external detuning parameter σ_2. In this case, the forcing amplitude is $f_1=0.025$, the modal damping is $\mu_i=0.05$ and the internal detuning parameter is $\sigma_1=0.04$. The response curve corresponding to the first amplitude shows a noticeable hardening-spring type behavior (Fig. 4a). The modal amplitude of the indirectly excited second mode is smaller in comparison with the first mode (Fig. 4b). In the Figures (dotted) lines denote (unstable) stable equilibrium solutions and thin solid lines denote unstable foci.

As it is seen, the response curves exhibit an interesting behavior due to saddle-node bifurcations (where one of the corresponding eigenvalues crosses the imaginary axis along the real axis from the left- to the right-half plane) and Hopf bifurcations (where one pair of complex conjugate eigenvalues crosses the imaginary axis transversely from the left to the right-half plane). As σ_2 increases from a small value, the solution increases in amplitude and loses stability via a Hopf bifurcation at $\sigma_2=-0.2570$ (H_1) and regains its stability via a reverse Hopf bifurcation at $\sigma_2=-0.1598$ (H_2). Then, the response jumps to another branches of stable equilibrium solutions (jump effect), depending on the initial conditions. The dynamics solutions that emerge from this bifurcation will be analyzed in the next section. There is an unstable solution happening between two saddle-node bifurcations SN_1 and SN_2 ($\sigma_2=-0.1597$ and $\sigma_2=-0.1694$). The reduction in amplitude of the first mode represents an increased in the second mode amplitude. Increasing σ_2 beyond SN_2, the stable solution grows again in amplitude until arriving to a saddle-node bifurcation SN_3 ($\sigma_2=0.8279$), resulting in a jump of the response to another branches of solutions. The new stable branch is left bounded by a saddle-node bifurcation SN_4 ($\sigma_2=0.2330$).

The influence modal damping is shown in Fig. 5a and b. The modal damping is reduced to $\mu_i=0.025$, conserving the same forcing amplitude and internal detuning parameter values as in the previous model. It is observed that the curves are similar to the previous case, but the modal amplitudes result to be larger. However, it can be seen that the influence of the first mode on the second mode response is smaller in the neighborhood of the Hopf bifurcation H_1 and the saddle-node SN_2.

The influence of the load amplitude parameter f_1 on the frequency–response is analyzed in Fig. 6a–f, where the modal damping considered is $\mu_i=0.05$ and the internal detuning
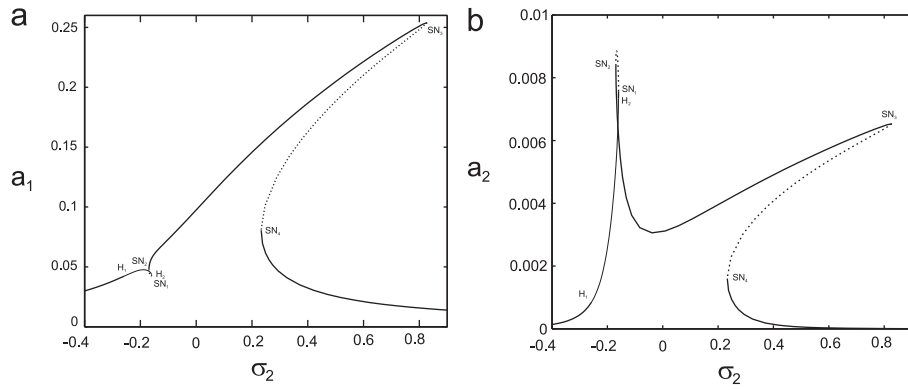
Fig. 4. Frequency–response curves for: (a) first and (b) second modes, when $f_1=0.025$, $\sigma_1=0.04$ and $\mu_i=0.05$. Solid (dotted) lines denote stable (unstable) equilibrium solutions and thin solid lines denote unstable foci.
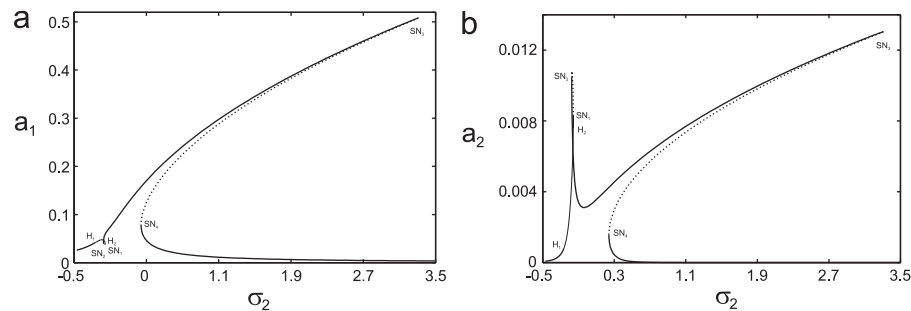

Fig. 5. Frequency–response curves for: (a) first and (b) second modes, when $f_1=0.05$, $\sigma_1=0.04$ and $\mu_i=0.025$. Solid (dotted) lines denote stable (unstable) equilibrium solutions and thin solid lines denote unstable foci.

parameter is far from the perfect resonance condition $\sigma_1=4$. When $f_1=0.05$, see Fig. 6a and b, the frequency–response curves are similar to the previous case. However, for large values of σ_2, the stable equilibrium solution loses stability via a Hopf bifurcation at $\sigma_2=0.756$ (H_3) and regains its stability via a reverse Hopf bifurcation at $\sigma_2=0.908$ (H_4). The curves for a forcing load $f_1=0.025$ are shown in Fig. 6c and d, and for $f_1=0.01$ in Fig. 6e and f. It can be seen that the amplitude of the second mode keeps almost the same when the load parameter is reduced. However, the dynamic behavior of the beam becomes more complicated and the hardening-spring curvature declines.

5.2. Dynamic solutions

According to the Hopf bifurcation theorem, small limit cycles are born as a result of the Hopf bifurcation. The born limit cycles are stable if the bifurcation is supercritical and unstable if the bifurcation is subcritical. Cycle-limit of the modulation equations corresponds to aperiodic responses of the beam. Fig. 7 shows a bifurcation diagrams for the orbits of the modulation Eqs. (43)–(46) in the neighborhood of the unstable foci, when $f_1=0.025$, $\sigma_1=0.04$ and $\mu_i=0.05$ (see Fig. 4). Full filled and empty circles denote branches of stable and unstable limit cycles. In addition, some phase portraits in the p1–p2 plane, characterizing the period-one limit cycles found on each branch, are shown in Fig. 7. It is observed that a stable small limit cycle born due to the supercritical Hopf bifurcation at H_1 ($\sigma_2=-0.257$). Then, as σ_2 increases, the limit cycle grows and loses stability through a cyclic-fold bifurcation at CF_1 ($\sigma_2=-0.241$). Consequently, the two-period quasiperiod response of the beam jumps to another two-period quasiperiod response. This stable branch is limited to the left and to the right by two cyclic-fold bifurcation CF_2 and CF_3 ($\sigma_2=-0.2511$ and $\sigma_2=-0.1673$, respectively). Increasing σ_2 after CF_3 the dynamic response jumps to a periodic solution.

On the other hand, as σ_2 decreases past the supercritical Hopf bifurcation H_2 ($\sigma_2=-0.159835$), the equilibrium solutions loses stability and gives way to a small-amplitude limit cycle. In Fig. 8, we show a schematic bifurcation diagrams for the orbits of the modulation equations, in the neighborhood of the Hopf bifurcation H_2. As the parameter σ_2 is reduced, the limit cycle grows, as shown in Fig. 8. It then goes through a sequence of cyclic-fold y doubling period bifurcation. When the stable solution encounters a cycle-fold bifurcation, the beam response jumps to a two-period quasiperiodic motion. When σ_2 decreases past CF in the last branch (denoted as VIII in Fig. 8), the beam response jumps to a periodic solution.

As it was observed in the previous section, the dynamic behavior of the beam becomes more complicated for an internal detuning parameter $\sigma_1=4$. The dynamic solutions for the case of $f_1=0.05$ and $\mu_i=0.05$ are analyzed (according to the frequency–response curves, Fig. 6a and b). In this case, there are four Hopf bifurcations, where H_1 ($\sigma_2=0.04025$) and H_3 ($\sigma_2=0.756$) correspond to supercritical Hopf bifurcation, while H_2 ($\sigma_2=0.5667$) and H_4 ($\sigma_2=0.908$) correspond to subcritical Hopf bifurcation.

Two schematic diagrams of dynamic solutions are shown in Figs. 9 and 10. As σ_2 increases from the left Hopf bifurcation H_1, nine branches of solutions are found in the neighborhood of H_1. It is noticeable that multiple attractors coexist between these branches. The relative sizes of branches of limit cycles in the neighborhood of the Hopf bifurcation H_1 are: $0.04025<\sigma_2<0.04713$ on branch I, $0.06757<\sigma_2<0.06762$ on branch II, $0.1528<\sigma_2<0.1722$ on branch III, $0.0447700<\sigma_2<0.0447733$ on branch IV, $-0.0148<\sigma_2<-0.013866$ on branch V, $-0.04594<\sigma_2<-0.04541$ on branch VI, $-0.07981<\sigma_2<-0.079525$ on branch VII, $-0.4489<\sigma_2<-0.44818$ on branch VIII and $-0.8389<\sigma_2<-0.826465$ on branch IX.

In the first branch, a small limit cycle born as a result of the supercritical Hopf bifurcation H_1. Two-dimensional projections of
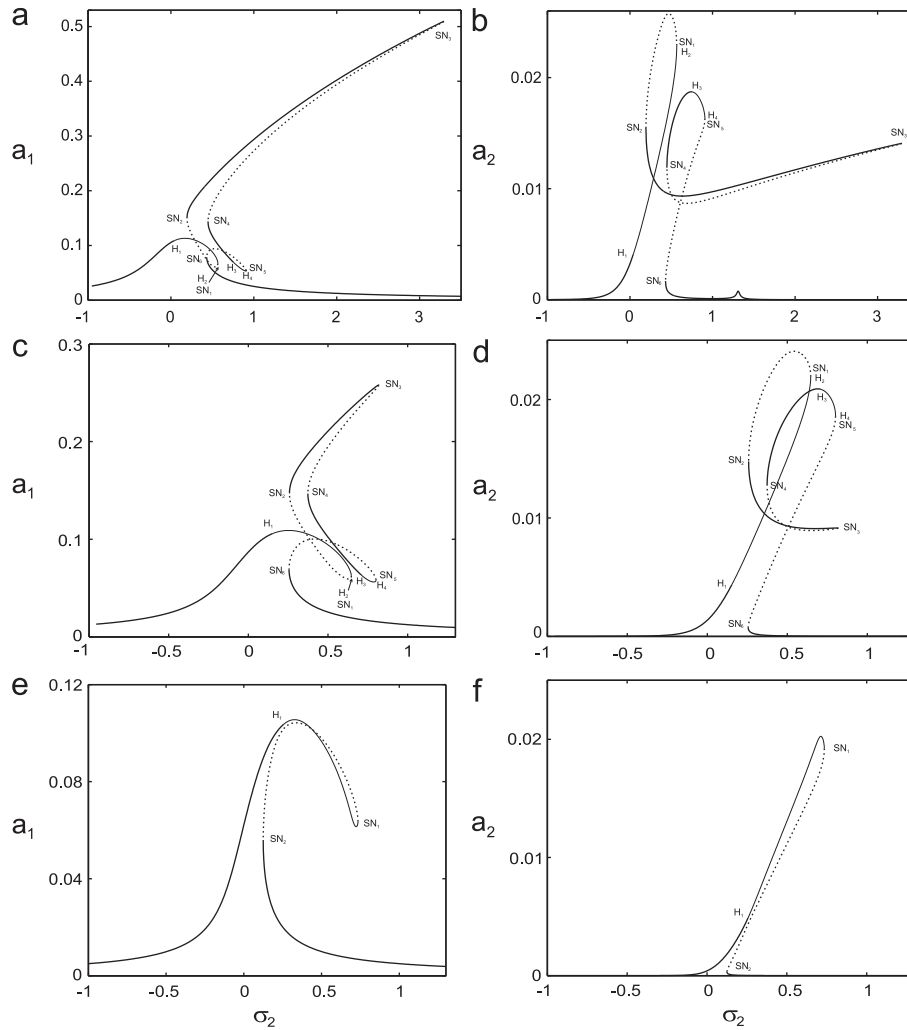
Fig. 6. Frequency–response curves for the first and second modes when $\mu_i=0.05$ and $\sigma_1=4$; (a and b) $f_1=0.1$, (c and d) $f_1=0.05$, (e and f) $f_1=0.025$. Solid (dotted) lines denote stable (unstable) equilibrium solutions and thin solid lines denote unstable foci.
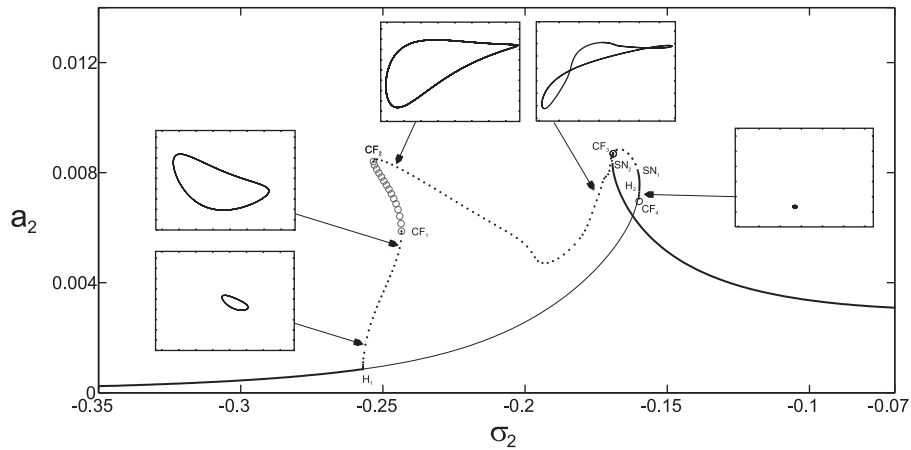

Fig. 7. Bifurcation diagrams, which limit cycle encounters between the Hopf bifurcation points when $\mu_i=0.05$, $\sigma_1=0.04$ and $f_1=0.025$. H=Hopf and CF=cycle-fold bifurcation. (●●●) Stable limit cycle, (○○○) unstable limit cycle. Solid (dotted) lines denote stable (unstable) equilibrium solutions and thin solid lines denote unstable foci.

the phase portraits of the limit cycle onto the p_1–p_2 plane at various pre and post-period-doubling bifurcation points are shown in Fig. 11a–f. The period-one limit cycle (Fig. 11a and b) grows and deforms and remains stable until a period-doubling bifurcation occurs PD_2 ($\sigma_2=0.0462763$). Then it undergoes a

sequence of period doubling bifurcations DP_4 ($\sigma_2=0.0470266$), DP_8 ($\sigma_2=0.0471067$), DP_{16} ($\sigma_2=0.04713062$), culminating in a chaotic attractor as shown in Fig. 12a ($\sigma_2=0.04718$). As σ_2 increases slightly, the chaotic attractor increases in size and collides with its basin boundary, resulting in the destruction of
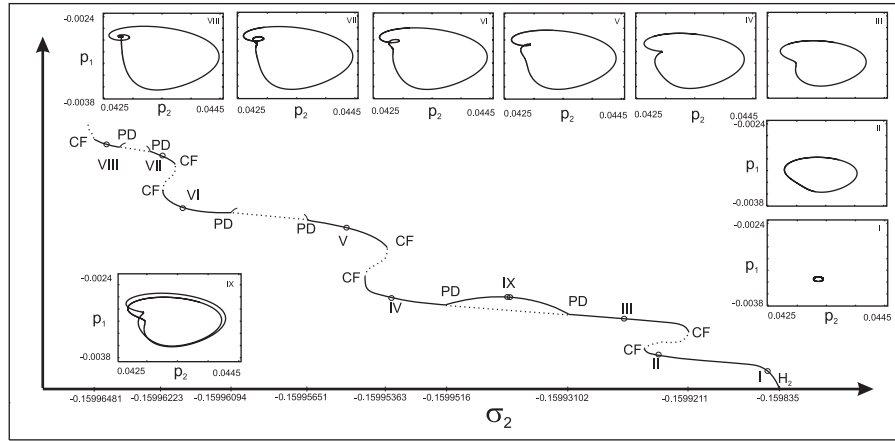
Fig. 8. Schematic of the dynamic solutions found in the neighborhood of the Hopf bifurcation H_2, when $\mu_i=0.05$, $\sigma_1=0.04$ and $f_1=0.025$. H=Hopf bifurcation, CF=cycle-fold bifurcation and PD=period-doubling bifurcation. (—) Stable and (…) unstable limit cycles.
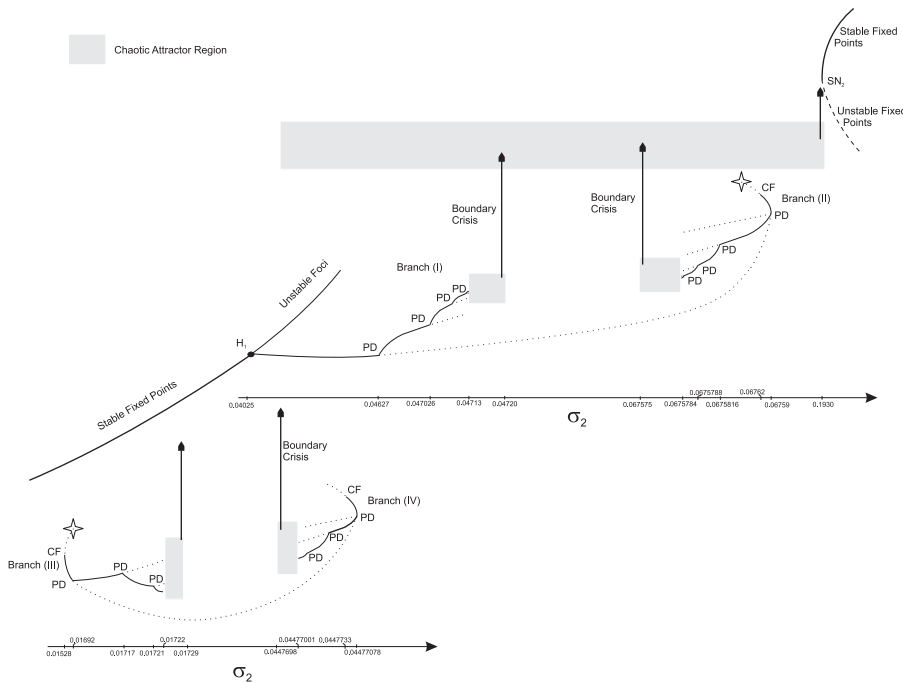

Fig. 9. Schematic of the dynamic solutions of branches I, II, III and IV found in the neighborhood of the Hopf bifurcation H_1, when $\mu_i=0.05$, $\sigma_1=4$ and $f_1=0.05$. H=Hopf bifurcation, CF=cycle-fold bifurcation and PD=period-doubling bifurcation. (—) Stable and (…) unstable limit cycles.

the chaotic attractor and its basin boundary in a boundary crisis. As a result, the beam response jumps to a far away attractor, as it can be seen in the time history of p_1 in Fig.12b. Two-dimensional projection of the large attractor is shown in Fig. 12c for a $\sigma_2=0.19$. Then, as σ_2 is increased further, the large chaotic attractor undergoes a boundary crisis and tends to a periodic solution in the neighborhood of SN_2 ($\sigma_2=0.0193$, see Fig. 9).

On the isolated branch II (see Fig. 9), a symmetric limit cycle was found at $\sigma_2=0.067596$ (see Fig.13a), through simulation of the modulation equations. As σ_2 is increased, the limit cycle encounters a cyclic fold bifurcation at $\sigma_2=0.06762$, causing the response to jump to the large chaotic attractor from the Branch I. As σ_2 is decreased, the symmetric limit cycle grows, and goes through a period bifurcation at $\sigma_2=0.06759$, as seen in the schematic diagram in Fig. 9. Two-dimensional projections of the phase portraits of the limit cycles found on branch II are shown in Fig. 13. The limit cycles of period-2 and period-4 are shown in Fig. 13b and c. Then, the chaotic attractor found in this branch

(see Fig. 13d) remains stable in size to $\sigma_2=0.067575$, after that value the response of the beam jumps to the large chaotic attractor found in branch I.

A similar dynamic behavior is observed in all the others branches. For example, the limit cycle found in the branch III is limited to the left by a cycle fold bifurcation (CF) at $\sigma_2=0.01528$ and to the right by a period-doubling bifurcation (PD) $\sigma_2=0.01692$. The two-dimensional projections of the phase portraits of the period-1 limit cycle for $\sigma_2=0.016775$ is shown onto the p_1–p_2 plane in the Fig. 14a. In this case, as σ_2 is decreased until CF, the beam response jumps to a periodic solution (see Fig. 9). Fig. 14 b–d, show the two-dimensional projections of the phase portraits of the limit cycles of period -2, -4 and -8 onto the p_1–p_2 plane corresponding to different values of the internal detuning parameter σ_2. These limit cycles are obtained increasing σ_2 further the PD bifurcation. The chaotic attractor found in this branch undergoes a boundary crisis at $\sigma_2=0.01729$ and the beam response jumps to a periodic solution (see Fig. 9). The limit cycles
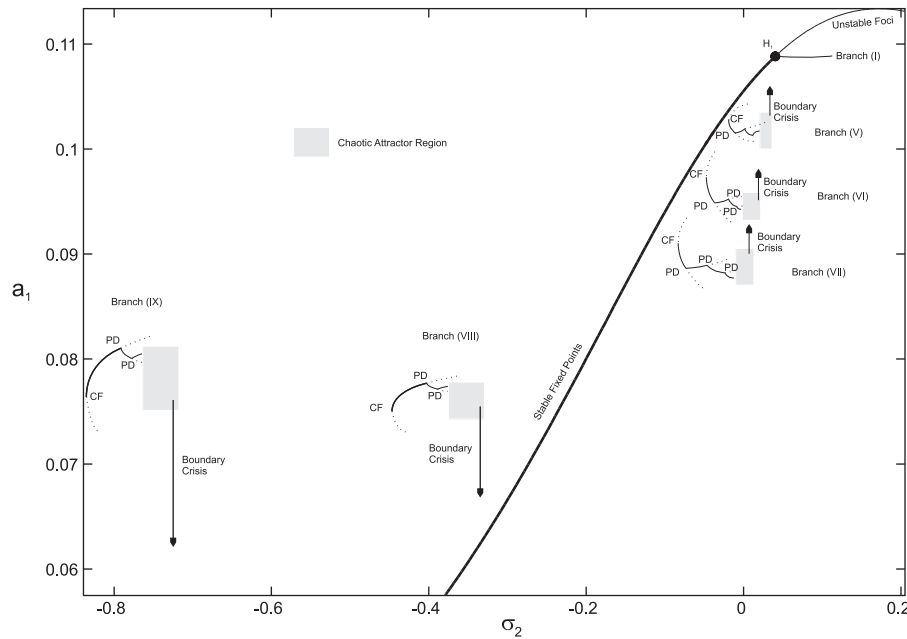
Fig. 10. Schematic of the dynamic solutions of branches V, VI, VII, VIII and IX found in the neighborhood of the Hopf bifurcation H_1, when $\mu_i=0.05$, $\sigma_1=4$ and $f_1=0.05$. H=Hopf bifurcation, CF=cycle-fold bifurcation and PD=period-doubling bifurcation. (—) Stable and (…) unstable limit cycles.
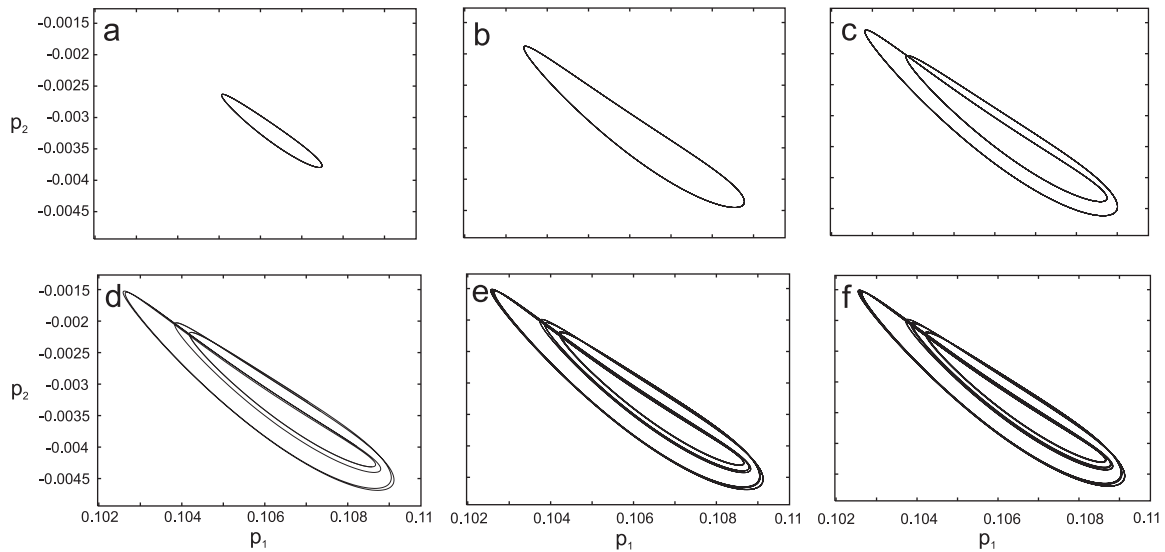

Fig.11. Two-dimensional projections of the phase portraits of the limit cycle found on branch I onto the p_1–p_2 plane, when $\mu_i=0.05$, $\sigma_1=4$, $f_1=0.05$ and $\sigma_2=$(a) 0.04146 (p-1), $\sigma_2=$(b) 0.04592 (p-1), $\sigma_2=$(c) 0.04669 (p-2), $\sigma_2=$(d) 0.04708 (p-4), $\sigma_2=$(e) 0.04712 (p-8) and $\sigma_2=$(f) 0.04713 (p-16).
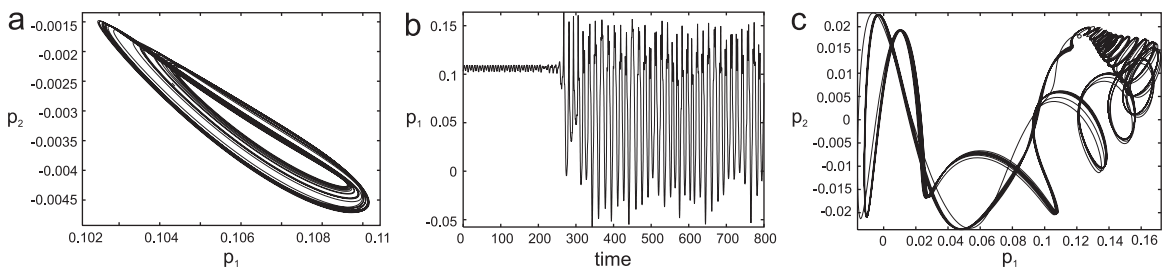

Fig. 12. Attractor chaotic found in branch I, two-dimensional projection of the phase portrait onto the p_1-p_2 plane showing the chaotic attractor before and after the explosive bifurcation for (a) $\sigma_2=0.0478$ and (c) $\sigma_2=0.19$, and (b) time history of p_1 after a crisis had occurred for $\sigma_2=0.0472$.

corresponding to branch IV, V, VI, VII, VIII and IX, are very similar to those showed in Fig. 14. For that reason they are not presented in the article.

On the other hand, there is another supercritical Hopf bifurcation denoted as H_3 ($\sigma_2=0.7558$) in the frequency–response of Fig. 6a and b. In this case, when σ_2 increases from the saddle node
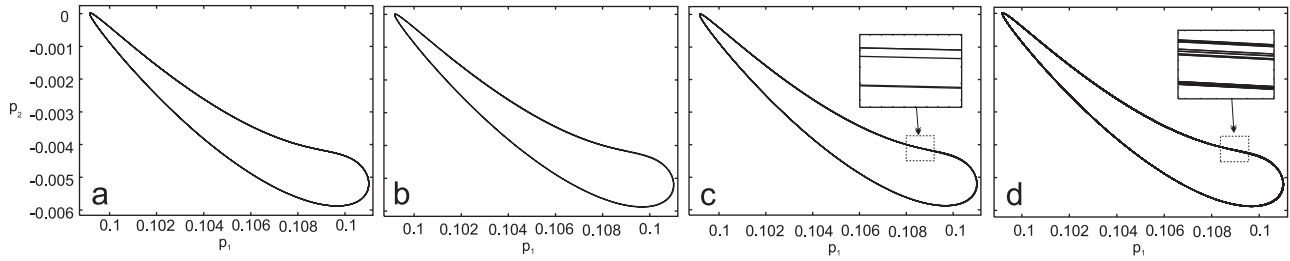
Fig. 13. Two-dimensional projections of the phase portraits of the limit cycle found on branch II onto the p_1-p_2 plane, when $\sigma_2 =$(a) 0.067596 (p-1), $\sigma_2 =$(b) 0.067584 (p-2), $\sigma_2 =$(c) 0.0675793 (p-4), $\sigma_2 =$(d) 0.0675784 (attractor).
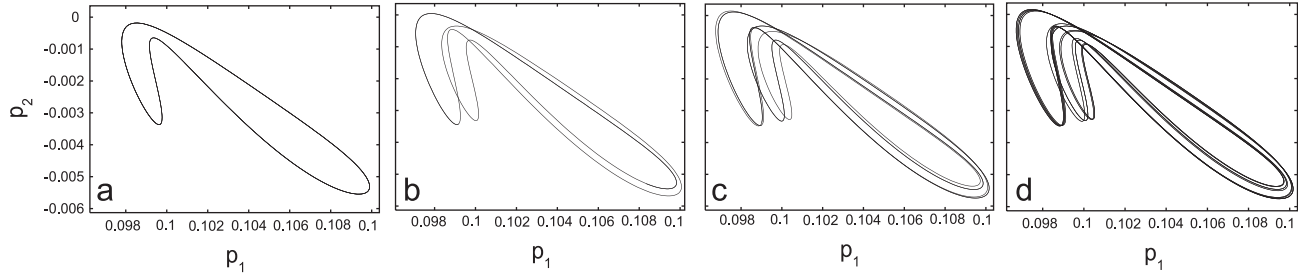

Fig. 14. Two-dimensional projections of the phase portraits of the limit cycle found on branch III onto the p_1-p_2 plane, when $\sigma_2 =$(a) 0.01677489 (p-1), $\sigma_2 =$(b) 0.01703596 (p-2), $\sigma_2 =$(c) 0.01721368 (p-4), $\sigma_2 =$(d) 0.01722902 (attractor).
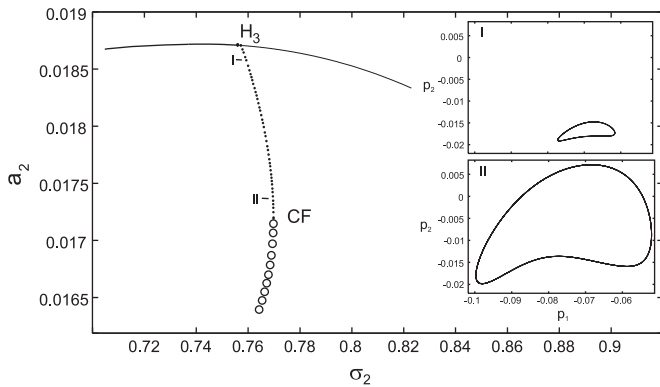

Fig. 15. Bifurcation diagrams in the neighborhood of the Hopf bifurcation H_3. H=Hopf and CF=cycle-fold bifurcation. (●●●) Stable limit cycle, (○○○) unstable limit cycle. Solid lines denote stable equilibrium solutions and thin solid lines denote unstable foci.

bifurcation SN_4, a small limit cycle born as a result of the supercritical Hopf bifurcation, which grows and loses stability via a cycle-fold bifurcation CF at $\sigma_2 = 0.7698$. Consequently, the quasiperiodic response of the beam jumps to a periodic motion. A schematic diagram of bifurcation is shown in Fig. 15. The limit cycles found in this branch are also shown.

6. Conclusions

The nonlinear planar response of a cantilever rotating box beam to a principal parametric resonance of its first flexural mode is investigated. The beam is subjected to a harmonic transverse load in the presence of internal resonance. The internal resonance can be activated for a range of the beam rotating speed, where the second natural frequency is approximately three times the first natural frequency. Geometric cubic nonlinear terms are included in the equation of motion due to midline stretching of the beam. The FGMs thermo-mechanical properties vary smoothly and continuously in predetermined directions throughout the body of the structure.

By means of the method of multiple scales applied directly on the partial-differential equation four first-order nonlinear ordinary-differential equations were derived, describing the modulation of the amplitudes and phases of the interacting modes. The frequency–response curves exhibit a hardening type behavior. When the excitation frequency is slowly varied, the response may undergo saddle-node and Hopf bifurcations. On the other hand, when the internal detuning parameter is varied from its perfect condition, the frequency–response curves exhibit a more complex behavior. It was shown that this effect is also influenced by the load amplitude parameter value. In this case, it was found that the modulation equations posses complex dynamics, including supercritical period-doubling bifurcation, the coexistence of multiple attractors, and various jump responses driven by cyclic-fold bifurcation, subcritical period-doubling bifurcations, and boundary crises. The limit cycle solutions of the modulation equations may undergo a sequence of period-doubling bifurcations, culminating in chaos. The chaotic attractors may undergo attracting-merging and boundary crises. In a future work we will include the shear deformation effect on the beam model.

Acknowledgments

Appendix A

The terms used in Eqs. (39)–(41) are defined as:

$$\Gamma_1 = -2i\omega_1\phi_1(A_1' + \mu A_1) + \left(3\phi_1'' \int_0^1 \phi_1'^2 dx\right) A_1^2 \bar{A}_1$$
$$+ \left(2\phi_1'' \int_0^1 \phi_1'\phi_2' dx + \phi_2'' \int_0^1 \phi_1' 2 dx\right) A_2 \bar{A}_1^2 e^{i\sigma_1 T_1}$$
$$+ \left(4\phi_2'' \int_0^1 \phi_1'\phi_2' dx + 2\phi_2'' \int_0^1 \phi_2'^2 dx\right) A_1 A_2 \bar{A}_2 \qquad (50)$$

$$\Gamma_2 = -2i\omega_2\phi_2(A_2'' + \mu A_2) + \left(3\phi_2'' \int_0^1 \phi_2'^2 dx\right)A_2^2\bar{A}_2 + \left(\phi_1'' \int_0^1 \phi_1'^2 dx\right)A_1^3 e^{-i\sigma_1 T_1}$$

$$+ \left(4\phi_1'' \int_0^1 \phi_1'\phi_2' dx + 2\phi_2'' \int_0^1 \phi_1'2 dx\right)A_1 A_2 \bar{A}_1 \tag{51}$$

$$\mu_m = \int_0^1 \mu\phi_m^2 dx \tag{52}$$

$$\gamma_{mm} = \frac{3}{8\omega_m}\Gamma_{mmmm} \tag{53}$$

$$\gamma_{mn} = \frac{1}{8\omega_m}(4\Gamma_{mmnn} + 2\Gamma_{mnmn}), \quad m \neq n \tag{54}$$

$$\delta_1 = \frac{1}{8\omega_1}(2\Gamma_{1112} + \Gamma_{1211}) \tag{55}$$

$$\delta_2 = \frac{\Gamma_{2111}}{8\omega_2} \tag{56}$$

$$\Gamma_{mnpq} = -\left(\int_0^1 \phi_m\phi_n'' dx\right)\left(\int_0^1 \phi_p'\phi_q' dx\right) \tag{57}$$

$$f_m = \frac{1}{\omega_m}\int_0^1 f(x)\phi_m dx \tag{58}$$

References

[1] Schilhansl MJ. Bending frequency of a rotating cantilever beam. Journal of Applied Mechanics—ASME 1958;25:28–30.

[2] Wang JTS, Mahrenholtz O, Bohm J. Extended Galerkin's method for rotating beam vibrations using Legendre polynomials. Solid Mechanics Archives 1976;1:341–65.

[3] Leissa A. Vibrational aspects of rotating turbomachinery blades. Applied Mechanics Reviews 1981;34:629–35.

[4] Hodges DH, Rutkowski MJ. Free-vibration analysis of rotating beams by a variable-order finite-element method. AIAA Journal 1981;19:1459–66.

[5] Pesheck E, Pierre C, Shaw SW. Modal reduction of a nonlinear rotating beam through nonlinear normal modes. Journal of Vibration and Acoustics 2002;124:229–36.

[6] Pesheck E, Pierre C, Shaw SW. A new Galerkin-based approach for accurate nonlinear normal modes through invariant manifolds. Journal of Sound and Vibration 2002;246:971–93.

[7] Apiwattanalunggarn P, Shaw SW, Pierre C, Jiang D. Finite-element-based nonlinear modal reduction of a rotating beam with large-amplitude motion. Journal of Vibration and Control 2003;9:235–63.

[8] Turhan O, Bulut G. On nonlinear vibrations of a rotating beam. Journal of Sound and Vibration 2009;322:314–35.

[9] Shaw SW, Pierre C. Normal modes for non-linear vibratory systems. Journal of Sound and Vibration 1993;164:85–124.

[10] Shaw SW, Pierre C. Normal modes of vibration for non-linear continuous systems. Journal of Sound and Vibration 1994;169:319–47.

[11] Shaw SW, Pierre C, Pesheck E. Modal analysis-based reduced-order models for nonlinear structures—an invariant manifold approach. Shock and Vibration Digest 1999;31:3–16.

[12] Pesheck E, Pierre C, Shaw SW. Accurate reduced order models for a simple rotor blade model using nonlinear normal modes. Mathematical and Computer Modelling 2001;33:1085–97.

[13] Sankar BV. An elasticity solution for functionally graded beams. Composites Science and Technology 2001;61:689–96.

[14] Chakraborty A, Gopalakrishnan S, Reddy JN. A new beam finite element for the analysis of functionally graded materials. International Journal of Mechanical Sciences 2003;45:519–39.

[15] Kapuria S, Bhattacharyya M, Kumar AN. Bending and free vibration response of layered functionally graded beams: a theoretical model and its experimental validation. Composite Structures 2008;82:390–402.

[16] Piovan MT, Sampaio R. A study on the dynamics of rotating beams with functionally graded properties. Journal of Sound and Vibration 2009;327:134–43.

[17] Piovan MT, Sampaio R. Vibrations of axially moving flexible beams made of functionally graded materials. Thin-Walled Structures 2008;46:112–21.

[18] Oh SY, Librescu L, Song O. Thermoelastic modeling and vibrations of functionally graded thin-walled rotating blades. AIAA Journal 2003;41:2051–60.

[19] Oh SY, Librescu L, Song O. Vibration and instability of functionally graded circular cylindrical spinning thin-walled beams. Journal of Sound and Vibration 2005;285:1071–91.

[20] Fazelzadeh SA, Malekzadeh P, Zahedinejad P, Hosseini M. Vibration analysis of functionally graded thin-walled rotating blades under high temperature supersonic flow using the differential quadrature method. Journal of Sound and Vibration 2007;306:333–48.

[21] Fazelzadeh SA, Hosseini M. Aerothermoelastic behavior of supersonic rotating thin-walled beams made of functionally graded materials. Journal of Fluids and Structures 2007;23:1251–64.

[22] Nayfeh AH, Mook DT. Nonlinear oscillations. New York: Wiley; 1979.

[23] Nayfeh AH, Balachandran B. Modal interactions in dynamical and structural systems. Applied Mechanics Reviews 1989;42:175–201.

[24] Nayfeh AH. Nonlinear interactions. 1st ed. New York: Wiley; 1996.

[25] Chin CM, Nayfeh AH. Three-to-one internal resonance in hinged-clamped beams. Nonlinear Dynamics 1997;12:129–54.

[26] Nayfeh AH, Balachandran B. Applied nonlinear dynamics: analytical computational and experimental methods. 1st ed. New York: Wiley-Interscience; 1995.

[27] Zhao FQ, Wang ZM, Liu HZ. Thermal post-buckling analyses of functionally graded material rod. Applied Mathematics and Mechanics 2007;28:59–67.

[28] Malekzadeh P. Two-dimensional in-plane free vibrations of functionally graded circular arches with temperature-dependent properties. Composite Structures 2010;91:38–47.

[29] Reddy JN, Chin CD. Thermomechanical analysis of functionally graded cylinders and plates. Journal of Thermal Stresses 1998;26:593–626.

[30] Piovan MT, Machado SP. Thermoelastic dynamic stability of thin-walled beams with graded material properties. Thin-Walled Structures 2011;49:437–47.

[31] Tanigawa Y. Some basic thermoelastic problems for nonhomogeneous structural materials. Applied Mechanics Reviews 1995;48:287–300.

[32] Nayfeh AH, Mook DT, Nayfeh JF. Some aspects of modal interactions in the response of beams. AIAA paper no. 87-0777 presented at the AIAA 28th structures, structural dynamic and materials conference, Monterey, 1987, p. 6–8.